Erschienen in: Soft Matter ; 11 (2015), 28. - S. 5697-5704
https://dx.doi.org/10.1039/C4SM02790F

Soft Matter

PAPER

View Article Online
View Journal | View Issue

Cite this: *Soft Matter*, 2015, **11**, 5697

Stress–structure relation in dense colloidal melts under forward and instantaneous reversal of the shear

Amit Kumar Bhattacharjee†

Received 15th December 2014, Accepted 2nd June 2015

DOI: 10.1039/c4sm02790f

www.rsc.org/softmatter

A dense supercooled colloidal melt in forward shear from a quiescent state shows overshoot in the shear stress at 10% strain with an unchanged fluid structure at equal stress before and after overshoot. In addition, we find an overshoot in the normal stress with a monotonic increase in the osmotic pressure at an identical strain. The first and second normal stresses become comparable in magnitude and opposite in sign. A functional dependence of the steady state stress and osmotic pressure with the Péclet number demonstrates the signature of crossover between Newtonian and nearly-Newtonian regimes. Moreover, instantaneous shear reversal from a steady state exhibiting the Bauschinger effect, where a strong history dependence is observed depending on the time of the flow reversal. The distribution of the particulate stress and osmotic pressure at the point of the flow reversal is shown to be a signature of the subsequent response. We link the history dependence of the stress–strain curves to changes in the fluid structure measured through the angular components of the radial distribution function. A uniform compression in the transition from forward to reversed flowing states is found.

I. Introduction

The mechanical and structural response of a dense colloidal dispersion under external forces are intriguing due to the interplay of the associated single particle relaxation time scale τ_0 and the structural relaxation time scale τ, which is many orders of magnitude slower than the previous. A rich behaviour of amorphous solid like and non-Newtonian fluid like response is seen in experiments and simulations when perturbed on a timescale $1/\dot{\gamma}$ with $\tau_0 \ll \dot{\gamma}^{-1} \ll \tau$.[1] Fluid like behaviour is exemplified by an increase in the shear viscosity, referred to as shear thinning or thickening, while the solid like behaviour is through the finite yield stress and nonzero elastic constants of the media.[2] Non-Newtonian fluids also exhibit nonzero normal stress components, the signs of which can lead to compression or propulsion of the fluid mass leading to fascinating phenomena *e.g.* rotating rod flows[3] and rod climbing effects in attractive colloids.[4] The flowing steady state response is usually characterized as a nonlinear function of $\dot{\gamma}$ by the macroscopic shear stress σ_{xy}. In addition, the first and second normal stresses, together with the osmotic pressure as a function of $\dot{\gamma}$, must be sought to characterize the stress tensor. The nonlinear functional forms of the shear and normal stresses with the Péclet number, as well as a positive first normal stress and a sign reversed second normal stress, for monodisperse colloidal suspensions at lower and moderately high volume fractions have been reported in Stokesian dynamics simulations of concentrated colloidal suspensions[5] as well as molecular dynamics (MD) simulations of non-Brownian spheres.[6] Similar results have been reported in systems with charge-stabilized dispersion,[7] however the functional dependence in the vicinity of the glass transition are not known.

In addition to the study of steady state properties, rigorous theoretical, experimental and simulational emphases have been applied in the past couple of decades to study the transient response of various systems in external shear to understand the kinetic pathway through which these systems evolve to a steady flowing state. As a constant strain rate is applied to a quiescent state at $t = 0$, the shear stress increases from zero to a steady state value with an intermediate hump at 10% strain amplitude for dense colloids, known in the literature as stress overshoot. These overshoot phenomena are reported in the MD simulations and experiments of gels,[8] dense polymeric melts,[9] liquid crystalline polymers[10] and charged, as well as uncharged, dense colloidal melts.[11–13] The last example is reasonably well understood within the mode coupling theory (MCT) framework. An internal connection between the superdiffusive particulate motion and the jump in the local stress variances have been attributed to the stress overshoot.

A considerable emphasis has also been placed on understanding the connection between the shear-deformed microstructure

---

Fachbereich Physik, Universität Konstanz, 78457 Konstanz, Germany

† Present address: Courant Institute of Mathematical Sciences, New York University, New York, NY 10012, USA. E-mail: amitb@courant.nyu.edu.

and the macroscopic stresses.[14–16] A universal flow-induced structure at equal stresses has emerged at the elastic and plastic branch of the stress–strain curve. The application of shear deformation at a constant rate leads to a modification of the stress overshoot in a system quenched into its glassy state: after the startup flow, the shear is reversed in the steady state leading to a vanishing of the maximum in the stress–strain curve known as the Bauschinger effect.[12,17] The effect has been analyzed in terms of the anisotropic athermal elastic constants that arise since the initially isotropic amorphous state acquires anisotropy under the initial deformation. A gradual disappearance of the shear stress overshoot, as well as the cessation of the superdiffusion, is found by the successive flow reversal from intermediate states to the steady flowing state. The transient and steady state properties of the osmotic pressure are difficult to measure in experiments and have recently been computed in computer simulations.[18] To our knowledge, the transient and steady state response, in terms of the macroscopic quantities and their relation to the shear-deformed microstructure under various flow history, is yet to be sought.

Here we investigate the nonlinear rheology under the start up flow from the equilibrated state, as well as in the instantaneous flow reversal from the intermediate and steady flowing states, without referring to the athermal variant. The issues that we address here can be categorized into: (a) the transient and steady state response of the stresses and osmotic pressure to the steady shear and the response to the instantaneous reversal of the shear, (b) the connection between the Bauschinger effect and the particulate stresses and (c) the flow-induced structural response of the melt in transient and steady flowing states and their relation with the macroscopic stresses.

The article is organized as follows: Section II gives a concise overview of the simulation method while Section III preempts the results through an establishment of the connection between the mechanical response to the fluid microstructure. We discuss the central results in Section IV and Section V concludes.

II. Simulation methods

We simulate a model system of a dense supercooled colloidal suspension through nonequilibrium molecular dynamics simulation. An additive binary mixture of size ratio 1.2 is chosen to avoid crystallization, as well as artifacts due to large size disparity. The components interact within a cutoff distance $r < r_{c,\alpha\beta}(=2^{1/6}\sigma_{\alpha\beta})$ through a purely-repulsive soft-sphere WCA potential,[19] $V_{\alpha\beta}(r) = 4\varepsilon_{\alpha\beta}\left[\left(\frac{\sigma_{\alpha\beta}}{r}\right)^{12} - \left(\frac{\sigma_{\alpha\beta}}{r}\right)^{6} + \frac{1}{4}\right]S_{\alpha\beta}(r)$ where σ denotes the particle diameter and α and β the particle species. $S_{\alpha\beta}(r) = (r - r_{c,\alpha\beta})^4/[h^4 + (r - r_{c,\alpha\beta})^4]$ with $h = 10^{-2}\sigma_{\alpha\beta}$ being a smoothing function applied to ensure continuity of the force and conservation of the total energy in the *NVE* ensemble. Both species are assigned equal masses for convenience. The units of energy $\varepsilon_{\alpha\beta} = 1$ and the units of length are so chosen that $\sigma_{AA} = 1$ and the unit of time is $\tau = \sqrt{m_A \sigma_{AA}{}^2/\varepsilon_{AA}}$, where m_A is the mass of the A-species of the particles. The simulation consisted of $N = 2N_A = 1300$ particles in a three-dimensional box with a linear dimension $L = 10\sigma_{AA}$, corresponding to a number density $\rho = 1.3/\sigma_{AA}{}^3$.[12]

Colloidal properties are incorporated in the mixture by coupling to a dissipative particle dynamics (DPD) thermostat where the dissipative force, proportional to the relative velocity of two species of particles, ensures Galilean invariance and thereby the local conservation of momentum. The random force satisfying the fluctuation dissipation relation ensures a Boltzmann distribution in equilibrium. These two competing forces uniquely set the temperature of the system. The cut off radius for the thermostat is chosen to be $1.7r_{c,\alpha\alpha}$ and the controlling parameter for the frictional forces is set to $\zeta = 10$.

The Langevin equation of motion are integrated with a generalized velocity Verlet algorithm with a time increment of $\delta t = 5 \times 10^{-4}$. Our estimation of the glass transition point, according to the MCT description, is $T_c \approx 0.347$ and we focus our work on the equilibrated fluid at $T = 0.4$. The initial equilibration is proceeded by step increments of $\delta t = 10^{-3}$, assigning new velocities every 50 integration time steps. The simulation runs were long enough to observe the decay of the incoherent intermediate scattering function to zero for a wavenumber corresponding to a typical interparticle separation. A set of 1000 independently equilibrated configurations served as the initial configurations for the forward shear runs, while 1000 pre-sheared configurations for the three separate strains were chosen for the shear reversal runs, employing the DPD thermostat.

Shear is applied from the strain-free configurations in the x-direction with a gradient in the y-direction (thus, the vorticity is along z-direction) at an initial fixed strain rate of $\dot{\gamma} = 5 \times 10^{-3}$ for 3×10^7 steps, resulting in the steady state with a strain of $\gamma = 75$. Shear is reversed and proceeded from three pre-sheared states, denoted with strain $-\gamma_w^{el} = 3.5 \times 10^{-2}$, $-\gamma_w^{max} = 8.6 \times 10^{-2}$ and $-\gamma_w^{s} = 75$ for 3×10^7 simulation steps, resulting in steady states with accumulated strains of -74.965, -74.914 and 0. For all these cases, planar Couette flow is imposed by periodic Lees–Edwards boundaries and the establishment of a linear velocity profile is achieved within a few iterations.

III. Connection between stresses and microstructure

The amount of stress developed by the application of a steady shear to a quiescent unsheared state or pre-sheared states are measured through the nonzero components of the stress tensor $\boldsymbol{\sigma}_{\mu\nu}$. The Kirkwood formula defines a combination of kinematic and virial contributions to the stress tensor,[14]

$$\boldsymbol{\sigma}_{\mu\nu} = \langle \hat{\sigma}_{\mu\nu} \rangle = -\frac{1}{V}\left\langle \sum_{i=1}^{N}\left[m_i v_{i,\mu} v_{i,\nu} + \sum_{j \neq i} r_{ij,\mu} F_{ij,\nu} \right] \right\rangle \tag{1}$$

where the angular brackets are indicative of canonical averaging, i and j denote the particle index and μ and ν are the

Cartesian directions. In a specified coordinate system having shear along the x direction with a gradient along the y direction, the dominant contribution to the shear stress is the off-diagonal xy-element and the normal stresses are a combination of the diagonal xx, yy and zz-elements of the stress tensor. The first and second normal stresses are the differences in the diagonal components as,[2]

$$\mathcal{N}_1 = \langle \boldsymbol{\sigma}_{xx} - \boldsymbol{\sigma}_{yy} \rangle; \quad \mathcal{N}_2 = \langle \boldsymbol{\sigma}_{yy} - \boldsymbol{\sigma}_{zz} \rangle. \tag{2}$$

and the third normal stress $\mathcal{N}_3$ is the sum of the two. The osmotic pressure is the sum of the diagonal elements of the stress tensor,

$$\mathcal{P} = -\frac{1}{3}\langle \boldsymbol{\sigma}_{xx} + \boldsymbol{\sigma}_{yy} + \boldsymbol{\sigma}_{zz} \rangle. \tag{3}$$

The virial part of the stress tensor in eqn (1) can be expressed in terms of the pair distribution function $g^{\alpha\beta}(\mathbf{r}) = V/N_\alpha N_\beta \times \left\langle \sum_{i=1}^{N_\alpha} \sum_{j(\neq i)}^{N_\beta} \delta\left(\mathbf{r} - \left|\mathbf{r}_i^\alpha - \mathbf{r}_j^\beta\right|\right) \right\rangle$ by rewriting the equation and substituting expressions for the pairwise force in the following manner,[14]

$$\begin{aligned}
\boldsymbol{\sigma} &= -\frac{1}{2V}\left\langle \sum_{i=1}^{N_\alpha} \sum_{j(\neq i)}^{N_\beta} \mathbf{r}_{ij}\mathbf{F}_{ij} \right\rangle, \\
&= -\frac{1}{2V}\left\langle \int \mathrm{d}\mathbf{r} \sum_{\alpha,\beta} \sum_{i=1}^{N_\alpha} \sum_{j(\neq i)}^{N_\beta} \delta\left(\mathbf{r} - \left|\mathbf{r}_i^\alpha - \mathbf{r}_j^\beta\right|\right) \mathbf{r}\mathbf{F}_{ij} \right\rangle, \\
&= \frac{1}{2V}\left\langle \int \mathrm{d}\mathbf{r} \sum_{\alpha,\beta} \sum_{i=1}^{N_\alpha} \sum_{j(\neq i)}^{N_\beta} \delta\left(\mathbf{r} - \left|\mathbf{r}_i^\alpha - \mathbf{r}_j^\beta\right|\right) \frac{\mathbf{r}\mathbf{r}}{r}\frac{\partial V_{\alpha\beta}}{\partial r} \right\rangle, \\
&= \frac{1}{2V^2}\int \mathrm{d}\mathbf{r} \sum_{\alpha,\beta} N_\alpha N_\beta \frac{\mathbf{r}\mathbf{r}}{r}\frac{\partial V_{\alpha\beta}}{\partial r} g^{\alpha\beta}(\mathbf{r}) \\
&= \frac{\rho^2}{2}\int \mathrm{d}\mathbf{r} \sum_{\alpha,\beta} \frac{N_\alpha N_\beta}{N^2} \frac{\mathbf{r}\mathbf{r}}{r}\frac{\partial V_{\alpha\beta}}{\partial r} g^{\alpha\beta}(\mathbf{r})
\end{aligned} \tag{4}$$

where $\rho = N/V$ is the average density and N_α and N_β correspond to the number of particles of the respective species index.

The shear induced pair distribution function for either the forward or backward directed sheared states does not exhibit any significant structural change compared to the quiescent state. A more relevant quantity sensitive to shear is constructed[14–16] where the three dimensional pair correlation function is expanded into the basis of spherical harmonics as, $g^{\alpha\beta}(\mathbf{r}) = \sum_l \sum_m g_{lm}^{\alpha\beta}(r) Y_{lm}(\theta, \phi)$. Here $Y_{lm}(\theta,\phi) = (-1)^m \sqrt{\frac{2l+1}{4\pi}\frac{(l-m)!}{(l+m)!}} P_{lm}(\cos\theta)\mathrm{e}^{\mathrm{i}m\phi}$ are the spherical harmonics of degree l and order m, θ and ϕ are the polar and azimuthal angles and $P_{lm}(\cos\theta)$ is the associated Legendre polynomial.[20] From symmetry considerations, only even numbers of l are existent and the most relevant terms in the expansion are associated to $l = 2$ and $m = 0, \pm 2$. Here we look for in-plane structural changes to the shear and the relevant expansion coefficients associated to $g(r)$ are,

$$\begin{aligned}
\mathrm{Re}\left[g_{22}^{\alpha\beta}(r)\right] &= \sqrt{\frac{15}{16\pi}}\frac{V}{N_\alpha N_\beta}\left\langle \sum_{i=1}^{N_\alpha} \sum_{j(\neq i)}^{N_\beta} \delta\left(r - \left|\mathbf{r}_i^\alpha - \mathbf{r}_j^\beta\right|\right) \right. \\
&\quad \left. \times \frac{\left(x_i^\alpha - x_j^\beta\right)^2 - \left(y_i^\alpha - y_j^\beta\right)^2}{r^4} \right\rangle
\end{aligned} \tag{5}$$

$$\begin{aligned}
\mathrm{Im}\left[g_{22}^{\alpha\beta}(r)\right] &= \sqrt{\frac{15}{8\pi}}\frac{V}{N_\alpha N_\beta}\left\langle \sum_{i=1}^{N_\alpha} \sum_{j(\neq i)}^{N_\beta} \delta\left(r - \left|\mathbf{r}_i^\alpha - \mathbf{r}_j^\beta\right|\right) \right. \\
&\quad \left. \times \frac{\left(x_i^\alpha - x_j^\beta\right)\left(y_i^\alpha - y_j^\beta\right)^2}{r^4} \right\rangle
\end{aligned} \tag{6}$$

where Re and Im represent the real and imaginary parts. Both these components are nonexistent in the quiescent state while they accumulate values in the sheared states. Integrating the algebraic combination of these functions, together with the interparticle force, yields the first normal stress[21] as well as the shear stress,[16,21]

$$\mathcal{N}_1 = \rho^2\sqrt{\frac{2\pi}{15}}\sum_{\alpha\beta}\frac{N_\alpha N_\beta}{N^2}\int_0^\infty \mathrm{d}r\, r^3 \frac{\partial V_{\alpha\beta}(r)}{\partial r}\mathrm{Re}\left[g_{22}^{\alpha\beta}(r)\right], \tag{7}$$

$$\sigma_{xy} = -\rho^2\sqrt{\frac{2\pi}{15}}\sum_{\alpha\beta}\frac{N_\alpha N_\beta}{N^2}\int_0^\infty \mathrm{d}r\, r^3 \frac{\partial V_{\alpha\beta}(r)}{\partial r}\mathrm{Im}\left[g_{22}^{\alpha\beta}(r)\right]. \tag{8}$$

IV. Results

We summarize the main findings in the dynamics and microstructure of the colloidal melt under shear startup and instantaneous shear reversal.

A. Dynamics

1. Flow curve. Fig. 1 shows the flow curve, that is the steady state scaling of the shear stress, first and second normal stresses and the osmotic pressure with the corresponding Péclet number (Pe) in the forward shear at a fixed temperature $T = 0.4$. The structural relaxation timescale of the supercooled melt at this temperature is computed to be $\tau_\alpha = 1.8 \times 10^3$, which is slower by a factor of 10^4 than a single particle relaxation time. Panel (a) depicts an increase in σ_{xy} with increasing Pe, which is a typical mechanical response of the melt, with a crossover from a Newtonian to a sub-Newtonian scaling regime for Pe > 0.1, corresponding to strain rates higher than $\dot{\gamma} = 10^{-4}$. It is to be noted that above T_c, no finite yield stress exists and the low Pe response is always Newtonian, as expected in a dense liquid mixture. However, we find that both the first and second normal stresses remain in the sub-Newtonian regime for Pe > 1. As noted in the Fig. 1 caption on the power law scaling of stresses with Pe, the scaling exponents of the normal stresses are higher than the shear stress exponents. This results in a slower

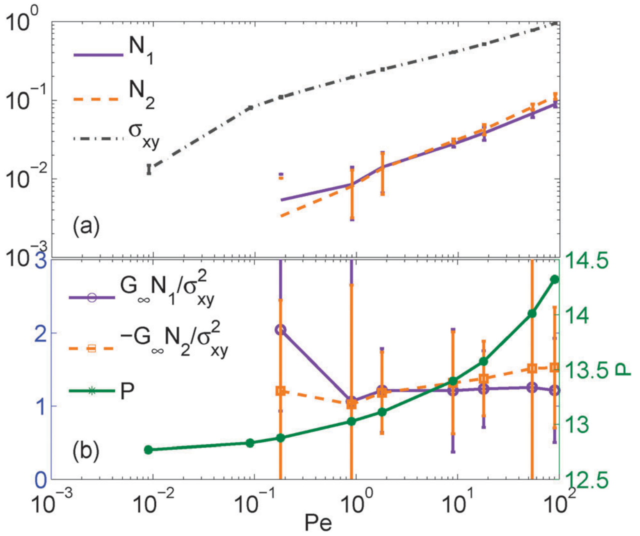

Fig. 1 Scaling of the steady state normal stresses $\mathcal{N}_{1,2}$, shear stress σ_{xy} [panel (a)] and osmotic pressure P [panel (b)] with the Péclet number Pe in forward shear. Panel (b) also shows the scaling of $G_\infty\mathcal{N}_{1,2}/\sigma_{xy}{}^2$ with Pe. The effective scaling laws are found to be $\sigma_{xy} \sim (\mathrm{Pe})^{0.36}$, $\mathcal{N}_1 \sim (\mathrm{Pe})^{0.51}$, $\mathcal{N}_2 \sim (\mathrm{Pe})^{0.58}$ and $P \sim (\mathrm{Pe})^{0.37}$ respectively. A total of 400 independent simulation runs are averaged for strain rates below 5×10^{-4} for the statistics while 100 averages were sufficient for the higher strain rates to obtain the graphics.

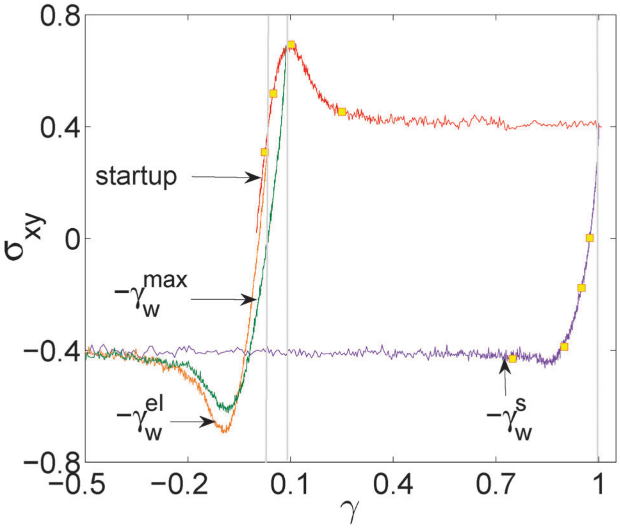

Fig. 2 Linear plot of stress–strain relation $\sigma_{xy}(\gamma)$ at fixed temperature and strain rate for various flow histories: (i) starting from equilibrium (startup, red), (ii) after the flow reversal in the steady state ($-\gamma_w^s$, purple), (iii) from the elastic regime ($-\gamma_w^{el}$, orange) and (iv) from the point of the stress overshoot ($-\gamma_w^{max}$, green). The abscissa of the $-\gamma_w^s$ curve is shifted from $\gamma = 75$ to $\gamma = 1$ for comparison. The vertical bars in gray denote the successive points of shear-reversal from elastic, overshoot and steady state regimes of the startup curve. The square (yellow) dots, corresponding to the accumulated strain indicated in Fig. 5, are printed on the startup and steady state reversed curves. A total of 200 independent configurations are averaged to obtain the graphics.

transition from a Newtonian to a sub-Newtonian regime for the normal stresses than the shear stress, thus explaining the depicted behaviour of the stresses at moderate values of Pe. We expect the low shear rate response of both stresses to be Newtonian. In panel (b), we depict the osmotic pressure as a function of Pe. The pressure decreases with decreasing Pe and saturates for Pe < 0.1. The low Pe response of the pressure is thus independent of Pe and reaches the quiescent state value. On the other hand, for moderately high values of Pe, the pressure and shear stress grows in a similar fashion, also reflected in the power law scaling exponents. A similar response in the pressure is also reported in simulations of hard-sphere glass.[22]

Another quantity of interest is the dimensionless number $G_\infty\mathcal{N}_{1,2}/\sigma_{xy}{}^2$ with G_∞ denoting the low frequency plateau modulus. For moderately high shear rates, the shear-thinning generalized Maxwell model predicts $\sigma_{xy} = G_\infty\gamma$ and $\mathcal{N}_{1,2} = 2G_\infty\gamma^2$ where γ is the strain. Therefore $G_\infty\mathcal{N}_{1,2}/\sigma_{xy}{}^2 = 2$.[23] The Pe-dependence of this quantity is displayed in panel (b). For an increasing Pe, the ratio progresses towards a value $\sim$2. This result thus restricts the applicability of the model at the considered range of Pe numbers.

2. **Shear stress response.** Next we draw our attention to studying the transient response of the melt under forward applied shear, and the instantaneous reversal of its direction. Fig. 2 depicts the shear stress as a function of strain $\gamma = \dot{\gamma}t$ for a fixed strain rate $\dot{\gamma}$ and time t. The stress is measured after the application of the strain rate to the equilibrated configurations and after the shear reversal from three different flowing states. With forward shear at a strain around $\gamma \approx 10\%$, a profound stress overshoot from the steady state stress value is observed, as found earlier in studies of binary colloidal melts with screened long ranged interactions.[11] The state-of-the-art explanation of this behaviour follows as the enhancement of energies transferred by the shearing forces to the particles caged within their immediate neighbours with a characteristic length: the Lindemann length. At any strain lower than the denoted strain, the mechanical response of the mixture is that of an elastic solid with finite G_∞ ($\sigma_{xy} \sim G_\infty\gamma$). Considering the time scales involved, the initial part of the $\sigma_{xy}(\gamma)$ curve for low strain rates is dominated by the long-time plateau modulus G_∞ rather than the instantaneous modulus G_0. At large strains however, the response is that of a viscous fluid where σ_{xy} is not a function of γ, but of $\dot{\gamma}$. Strains of order unity appear to be sufficient to drive the system into this state of steady flow. This is consistent with the expectation that the flow-induced decay of correlations occur on a time scale set by $\dot{\gamma}^{-1}$. The argument leading to this state follows as the release of elastic energy from the breaking of local cages, which also leads to superdiffusive particle motion in between the ballistic and diffusive motions, reported in the study of mean squared particle displacement.[11,12] Reversing the direction of the applied shear at various strains along the stress–strain curve results in an accumulated strain that first decreases to zero. After that, $|\gamma|$ grows linearly as a function of time. In the steady flowing state, the $|\gamma| \to \infty$ asymptote is $-\sigma_s(\dot{\gamma})$, where σ_s is the steady state stress at forward shear. Hence in Fig. 2, different $\sigma_{xy}(\gamma)$ curves in shear reversal coincide at large strains.

Comparing the steady state reversal curve with the initial startup curve, the most striking difference is the absence of a

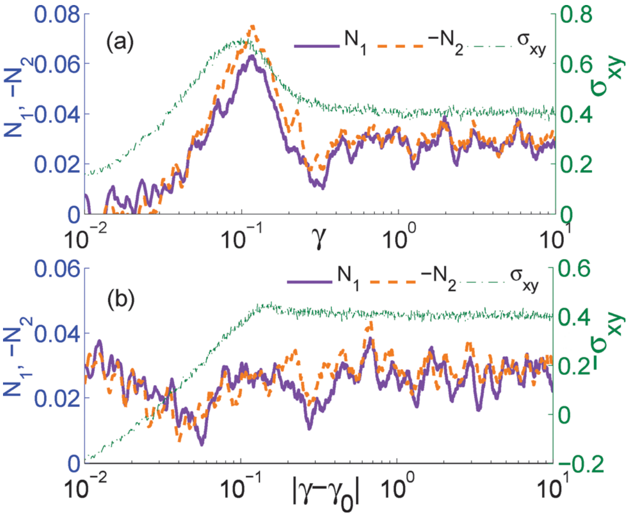

Fig. 3 Semilog plot of the normal stress–strain relation $\mathcal{N}_{1,2}(\gamma)$ at fixed temperature and strain rate for two different flow histories: panel (a): shear start up from a quiescent state and panel (b): shear reversal from a steady flowing state (denoted with $-\gamma_{\mathrm{w}}^{\mathrm{s}}$ in Fig. 2). For comparison, the shear stresses in both situations are depicted. A total of 1000 independent simulation runs are averaged to obtain the graphics.

stress overshoot. This agrees with the findings of ref. 17, where the same phenomenology was reported for a system quenched initially into the glassy state. As a consequence, the steady state value of the stress is reached earlier than the startup case at a value slightly higher than the accumulated strain of $|\gamma| \approx 0.1$. This is somewhat surprising, since one might expect the pre-sheared state to bear structural anisotropies that accommodate flow in the $+x$ direction and hence oppose that in the $-x$ direction more than the isotropic equilibrium structure. This appears not to be the case in our simulation, which we elaborate on more while discussing the local microstructure. This is also corroborated by looking at the instantaneous effective elastic modulus, $G_{\mathrm{eff}} = \mathrm{d}\sigma/\mathrm{d}\gamma|_{|\gamma-\gamma_0|=0.025}$ (γ_0 being the strain when the stress first decreases to zero): a lower value is found following flow reversal than the one characterizing the initial startup from the equilibrium configuration.[12]

Flow reversal for the elastic transient results in a stress–strain curve that exhibits a negative stress overshoot, displayed in Fig. 2 and labeled with $-\gamma_{\mathrm{w}}^{\mathrm{el}}$. The magnitude of the overshoot is identical to the initial startup flow. This exemplifies that during the elastic part, the strain-induced rearrangements are essentially reversible, unlike in the plastic regime of viscous flow. The figure also depicts the case of flow reversal, once the initial stress–strain curve has reached its maximum (the curve labeled with $-\gamma_{\mathrm{w}}^{\max}$). This intermediate case still exhibits a pronounced overshoot, albeit lower than the $-\gamma_{\mathrm{w}}^{\mathrm{el}}$ case. Thus, up to the stress overshoot, the response of the system to the initial flow is mainly reversible. This is consistent with the notion that the overshoot marks the nontrivial breaking of the nearest neighbour cages due to the imposed flow. We want to remind the reader that an overshoot in $\sigma_{xy}(\gamma)$ implies a dynamic shear modulus or microscopic stress autocorrelation function which exhibits overrelaxation: stresses do not simply decorrelate but, during the breaking of cages, are released in such a way that they briefly become anti-correlated during the process.[11]

3. Transient dynamics of normal stresses. To complete the discussion on stresses, we studied the transient and steady state responses of normal stresses, defined in eqn (2), as a function of the strain. Panel (a) of Fig. 3 depicts $\mathcal{N}_1$ and $\mathcal{N}_2$ as a function of the strain γ for the startup shear from a quiescent configuration, while panel (b) displays the results of the shear reversal from the steady state after the shear stress becomes negative. The magnitude of the normal stress is noted to be approximately one order smaller than that of the shear stress, which can be anticipated due to the quadratic scaling of the normal stress with Pe. For the startup case, $\mathcal{N}_1$ builds up to attain a steady state value after exhibiting an overshoot at around 10% of the strain, very similar to the shear stress–strain response. The amount of overshoot in shear or normal stresses stays constant compared to the steady state value. $\mathcal{N}_2$, however, exhibits a negative stress overshoot with a crossover from a transient to a steady state. Surprisingly, we find $\mathcal{N}_1 \sim -\mathcal{N}_2$ and $\mathcal{N}_3 = \mathcal{N}_1 + \mathcal{N}_2 \sim 0$. After reversing the flow direction from a steady flowing state, we find the response of the normal stresses to the shear unchanged. The nonzero values of $\mathcal{N}_2$ indicate that for the forward shear, the stress overshoot phenomena are not limited only to the shear direction, but they also have a signature in the two directions perpendicular to it. The unchanged magnitude and sign of the normal stresses at the shear reversal from the steady state are indicative of uniform normal forces, devoid of the flowing direction. The distinction of the history dependent response in the flow reversal is not primarily due to the swapped flow direction, but due to whether the microscopic structure is still close to its equilibrium configuration (and hence only deformed reversibly), or whether it is sufficiently close to the flowing configuration.

4. Local stress fluctuation and pressure. Further support for the hypothesis claimed in the above section comes from a study of the local stress fluctuations, initially suggested by Zausch *et al.*[16] Defining a local stress element as $\sigma_{xy}^{i} = -(1/V)\sum_{j\neq i} r_{ij,x}F_{ij,y}$, such that $\langle\sigma\rangle = \sigma_{\mathrm{pot}}$ is the potential part of the macroscopic stress, the distribution of these local stresses around their average value is computed. The panel (a) of Fig. 4 depicts the variance of σ_{xy}^{i} as a function of strain $|\gamma|$ in the forward shear from the quiescent state and the instantaneous reversal from the steady flowing state. As already noted in ref. 16, the initial equilibrium configuration is characterized by a variance that is significantly lower than that in the flowing steady state. A steep increase in stress variance around $\gamma \approx 0.1$ is found, which coincides with the stress overshoot, separating the reversible elastic regime from the irreversible plastic counterpart. Reversing the shear flow from the steady state regime (denoted with $-\gamma_{\mathrm{w}}^{\mathrm{s}}$), $\mathrm{var}(\sigma_{xy}^{i})$ essentially remains at the previously reached level, after exhibiting a small dip below $\gamma \leq 0.1$. In panel (b) of Fig. 4, the osmotic pressure is displayed for the flow startup and reversal from the steady state. For the startup case, the increase in the osmotic pressure from one state to another is found without any overshoot at a strain ≈ 0.1. In the case of the shear reversal,

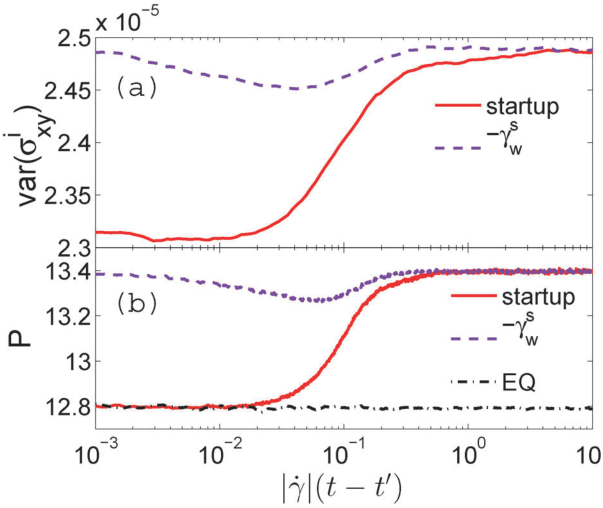

Fig. 4 Panel (a): variance of the local stress distribution corresponding to the stress–strain curves shown in Fig. 2. Panel (b): osmotic pressure for the shear startup and shear reversal from the steady state. The pressure at the quiescent state is also marked for comparison. A total of 1000 independent configurations are averaged to obtain the graphics.

the value remains constant at the previously attained value with a small dip. A plausible explanation for the dip can be sought by an argument that instantaneous shear reversal interrupts the established planar Couette flow, thus eventually lowering the fluctuations. The stress variance, as well as the pressure, reaches the forward steady state value as soon as the linear flow profile is re-established in the opposite direction. An identical response in the pressure and the fluctuation in the particulate stress with the strain indicates an interconnection between these seemingly different quantities.

B. Microstructure

1. Anisotropies in the transient structure. To understand the shear induced anisotropy in the local fluid structure, we measured the angle dependent radial distribution function $g(r,\theta)$ on the shear-gradient (x–y) plane. Fig. 5 shows the extra contribution of the shear to the microstructure from the homogeneous and isotropic quiescent state, denoted with g_{EQ}. A faint, orange arrow printed on panels (d) and (h) shows the extensional axis while a bold, purple arrow perpendicular to it in the same panels depicts the compressional axis. Successive points corresponding to the accumulated strain mentioned in Fig. 5 are printed in the stress–strain curve (Fig. 2) for a direct comparison. It is worth mentioning that planar Couette flow is established for all of the reported accumulated strains. As depicted in panels (a–d), in the forward shear the homogeneous state is steadily deformed with the development of anisotropies along the extension–compression axis. This feature of the shear induced structural deformation, which pushes more particles around the compressional axis while pulling the particles apart along the extensional axis, is also reported in molecular simulations.[15,24] As could be anticipated from the stress–strain relationship, the amount of compression–extension is the maximum at the point of stress overshoot (shown in panel (c)).

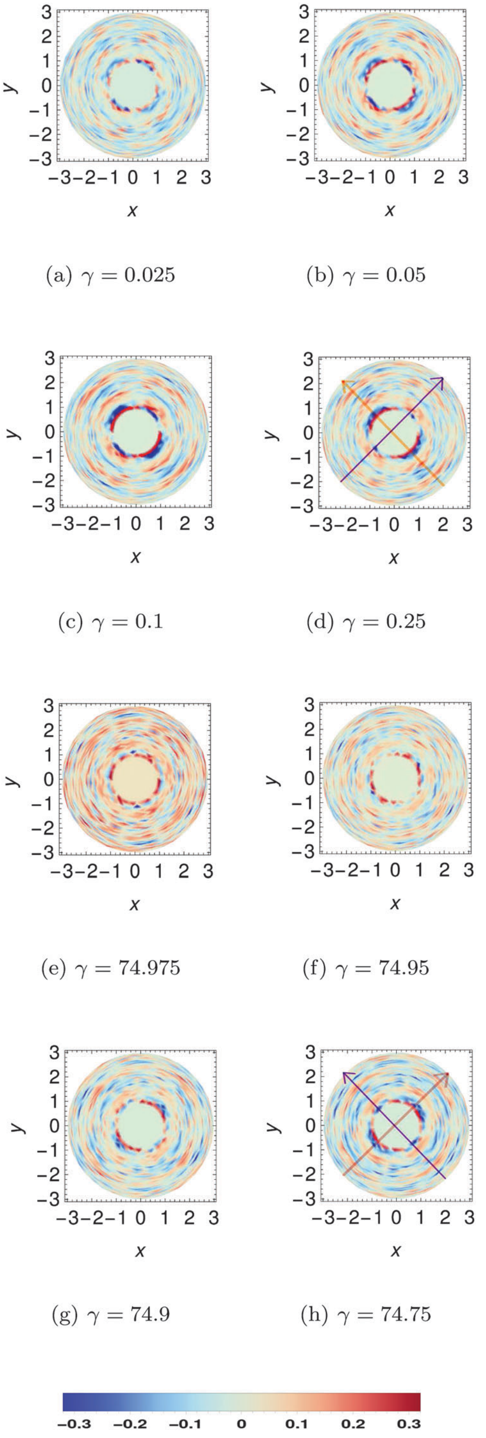

(a) $\gamma = 0.025$ (b) $\gamma = 0.05$

(c) $\gamma = 0.1$ (d) $\gamma = 0.25$

(e) $\gamma = 74.975$ (f) $\gamma = 74.95$

(g) $\gamma = 74.9$ (h) $\gamma = 74.75$

Fig. 5 Density plots of $g_{\mathrm{shear}}(r,\theta) - g_{\mathrm{EQ}}$ in the shear-gradient plain depicted in false colour. States after the shear startup from a quiescent state with accumulated strains are indicated in panels (a–d) while panels (e–h) show different states after the shear reversal from the plastic state with an accumulated strain γ = 75. In panels (d) and (h), the extension axis is displayed with a faint, orange arrow while the compression axis is displayed with a bold, purple arrow. A total of 100 independent simulation runs are averaged and, within each run, 10 configurations centered around the respective strain value are averaged to obtain the graphics.

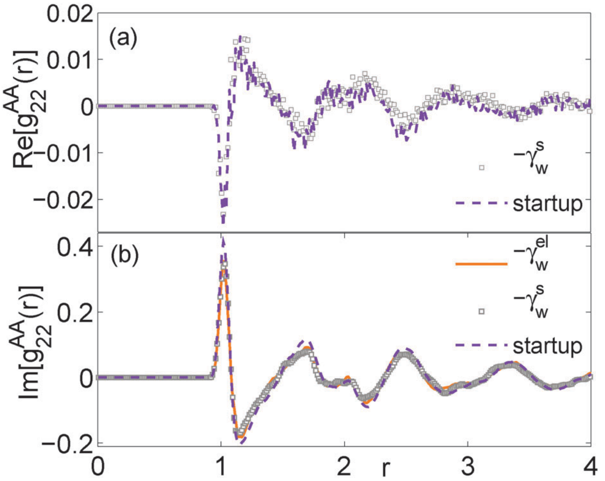

Fig. 6 Panel (a) shows steady state $\mathrm{Re}[g_{22}^{\alpha\alpha}(r)]$ correlations between $\alpha \in$ A-particles, obtained by correlating 250 steady state configurations within a strain window [50, 75] in a single run and then averaging over 20 independent samples for shear startup (purple, dashed line) and reversal from the plastic steady state (square symbol). Panel (b) shows the imaginary part of the $g_{22}^{\alpha\alpha}(r)$ correlations between $\alpha \in$ A-particles after shear reversal from the elastic (orange, solid line) and plastic branches (square symbol) at a steady state shear stress $\sigma_{xy} = -0.36$. The sign reversed forward steady state curve (purple, dashed line) is also shown for comparison.

Panels (e–h) depict the time evolution of the structure at a reversed flowing state. An instantaneous shear reversal from the steady state results in an exchange between the extension–compression axis with an intermediate uniformly compressed state, as seen in panel (e). This is clearly indicative of an absence of force chains or a jamming of colloidal particles[25] in the considered shear rate. The vanishing of the stress overshoot is attributed to the cessation of the maximal anisotropy along the compression–extension axis present in forward shear. Finally, panel (d) and panel (h) confirm the equivalence of the steady state structure in opposite flowing directions without any memory of the flow history.

2. **Steady state structure.** To conclude the discussion on the microstructure, we calculate the steady state structure observed in the local projected quantities $\mathrm{Re}[g_{22}^{\alpha\alpha}(r)]$ and $\mathrm{Im}[g_{22}^{\alpha\alpha}(r)]$ defined in eqn (5) and (6). Recall that the first normal stress can be obtained from $\mathrm{Re}[g_{22}^{\alpha\alpha}(r)]$ as $\mathcal{N}_1 = \rho^2\sqrt{2\pi/15}\sum_{\alpha\beta} N_\alpha N_\beta/N^2 \int_0^\infty \mathrm{d}r\, r^3 \left[\partial V_{\alpha\beta}(r)/\partial r\right] \times \mathrm{Re}\left[g_{22}^{\alpha\beta}(r)\right]$. The upper panel of Fig. 6 compares the steady state structure $\mathrm{Re}[g_{22}^{\alpha\alpha}(r)]$ for the shear startup from a quiescent state as well as the shear reversal from the steady state for $\alpha \in$ A-species. We find excellent agreement between the structure of the steady state for both directions, indicative of a homogeneously flowing state with an equal planar anisotropy devoid of any memory of the quiescent or pre-sheared configuration. The most important contribution to the first normal stress is attributed to the nearest neighbour distance structure of the pair correlator. As seen for the nearest neighbour distances, particles are squeezed along the compressional axis in the plane and extended along the extensional axis. This results in a positive $\mathcal{N}_1$ at the considered strain rate.

The shear stress on the other hand can be derived from $\mathrm{Im}[g_{22}^{\alpha\alpha}(r)]$ as $\sigma_{xy} = -\rho^2\sqrt{2\pi/15}\sum_{\alpha\beta} N_\alpha N_\beta/N^2 \int_0^\infty \mathrm{d}r\, r^3 \left[\partial V_{\alpha\beta}(r)/\partial r\right] \times \mathrm{Im}\left[g_{22}^{\alpha\beta}(r)\right]$. Panel (b) compares the positional dependence of $\mathrm{Im}[g_{22}^{\alpha\alpha}(r)]$ for $\alpha \in$ A-species at a steady state for two different shear reversal states, denoted by $-\gamma_w^{el}$ and $-\gamma_w^{s}$, to the forward directed steady state. The correlator (sign reversed) in the forward shear agrees well with the correlator obtained from the steady reversed flowing states. This result coincides with an earlier claim that at equal moduli of the shear stresses, the projected structure retains its shape devoid of the flow history.[16] We found this to hold for the reverse flowing states as well, thus extending the claim for the first normal stress–structure relation at a steady state and numerically validating eqn (7).

V. Conclusions and outlook

By employing a dissipative particle dynamics scheme in conjunction to the Lees–Edwards boundary condition to soft repulsive colloids, in this article we have discussed the nonlinear rheology of dense colloidal melts under shear flow, specifically the transient and steady state properties after a sudden application of a steady strain rate $\dot{\gamma}$, starting from either a quiescent state or various configurations which have been pre-sheared in the opposite direction. The functional dependence of shear and normal stresses, as well as osmotic pressure, with the Péclet number was sought. A crossover from a Newtonian to a sub-Newtonian regime is found in shear stress for $\mathrm{Pe} > 0.1$ while the normal stresses remain in the sub-Newtonian regime. The osmotic pressure saturates for lower Pe. The binary melt exhibits shear thinning and, for much higher strain rates, can result in a shear thickening behaviour with a negative $\mathcal{N}_1$.[26]

Stress–strain curves of the pre-sheared configurations are measured along with shear startup. In addition to the overshoot in shear stress, overshoot in the first and second normal stresses is observed at 10% strain amplitude with a step jump in the osmotic pressure as well as in the particulate stress variances. However, once the steady state is attained, no stress overshoot is found, while unchanged states of the pressure and local stress variance emerge in response to shear reversal. This validates the conjecture of shear induced nearest-neighbour cage breaking at startup flow, having a steady state with weak cages that ceases to play any dramatic role when the direction of flow is reversed. An interesting connection can be sought between the fluctuations of the particulate shear and normal stresses with the osmotic pressure, which is beyond the work presented here.

The angle dependent pair correlation function depicts that a uniform exchange of the compression–extension axis occurs with a continuous evolution of structure, obtaining a steady Couette flow in a relatively short span of time without cluttering or the formation of force chains which are a typical signature in athermal systems. We also do not find any shear induced crystallization at the considered shear rates. Maximal anisotropy is exhibited at a strain where stress overshoot appears in forward shear while such maxima cease to exist in the shear reversed states. The steady state structure in both directions containing an equal anisotropy confirms an absence of the flow history in the steady state. The agreement in the shear induced structure at a steady flowing state validates the relationship between the various components of the pair correlator and macroscopic stresses. The change of sign in the shear direction is attributed to an exchange of the extension–compression axis, as noted in the imaginary component of the pair distribution function, while the unchanged structure of the real component of the pair correlator confirms a positive $\mathcal{N}_1$ for both directions of the shear. In a similar spirit to eqn (7) and (8), the relation between $\mathcal{N}_2$ and the components of the pair correlator can be obtained[21] and an unchanged structure at equal stresses can be found. However, such studies should be performed at larger strain rates with the melt being quenched deeper into the glassy state, which is outside the scope of the presented work. We seek experimental measurements in dense supercooled melts to verify the claims presented in this article.

Acknowledgements

We thank Th. Voigtmann for several insightful suggestions and M. Fuchs, N. Wagner and R. Adhikari for useful discussions. We also thank P. Kuhn for providing the routine to calculate the angle dependent radial distribution function. We gratefully acknowledge funding through the Helmholtz Gesellschaft (HGF, VH-NG 406).

References

1 K. Binder and W. Kob, *Glassy materials and disordered solids: an introduction to their statistical mechanics*, World Scientific Pub. Co., Singapore, 2005.

2 R. G. Larson, *The structure and rheology of complex fluids*, Oxford University Press, New York, 1999.

3 F. Boyer, O. Pouliquen and E. Guazzelli, *J. Fluid Mech.*, 2011, **686**, 5.

4 T. F. F. Farage, J. Reinhardt and J. M. Brader, *Phys. Rev. E: Stat., Nonlinear, Soft Matter Phys.*, 2013, **88**, 042303.

5 T. N. Phung, J. F. Brady and G. Bossis, *J. Fluid Mech.*, 1996, **313**, 181.

6 J. Seth, L. Mohan, C. Champagne, M. Cloitre and R. Bonnecaze, *Nat. Mater.*, 2012, **10**, 838.

7 S. R. Rastogi, N. J. Wagner and S. R. Lustig, *J. Chem. Phys.*, 1996, **104**, 9234.

8 N. Koumakis, P. Ballesta, R. Besseling, W. C. K. Poon, J. F. Brady and G. Petekidis, *AIP Conf. Proc.*, 2013, **1518**, 365.

9 J. D. Moore, S. T. Cui, H. D. Cochran and P. T. Cummings, *Phys. Rev. E: Stat. Phys., Plasmas, Fluids, Relat. Interdiscip. Top.*, 1999, **60**, 6956.

10 Y.-G. Tao, W. K. den Otter and W. J. Briels, *Macromolecules*, 2006, **39**, 5939.

11 J. Zausch, J. Horbach, M. Laurati, S. U. Egelhaaf, J. M. Brader, T. Voigtmann and M. Fuchs, *J. Phys.: Condens. Matter*, 2008, **20**, 404210.

12 F. Frahsa, A. K. Bhattacharjee, J. Horbach, M. Fuchs and T. Voigtmann, *J. Chem. Phys.*, 2013, **138**, 12A513.

13 N. Koumakis, A. B. Schofield and G. Petekidis, *Soft Matter*, 2008, **4**, 2008.

14 J. G. Kirkwood, *J. Chem. Phys.*, 1946, **14**, 180.

15 H. J. M. Hanley, J. C. Rainwater and S. Hess, *Phys. Rev. A: At., Mol., Opt. Phys.*, 1987, **36**, 1795.

16 J. Zausch and J. Horbach, *Europhys. Lett.*, 2009, **88**, 60001.

17 S. Karmakar, E. Lerner and I. Procaccia, *Phys. Rev. E: Stat., Nonlinear, Soft Matter Phys.*, 2010, **82**, 026104.

18 J. M. Brader, M. Siebenbürger, M. Ballauff, K. Reinheimer, M. Wilhelm, S. J. Frey, F. Weysser and M. Fuchs, *Phys. Rev. E: Stat., Nonlinear, Soft Matter Phys.*, 2010, **82**, 061401.

19 J. D. Weeks, D. Chandler and H. C. Andersen, *J. Chem. Phys.*, 1971, **54**, 5237.

20 M. Abramowitz and I. A. Stegun, *Handbook of Mathematical Functions: With Formulas, Graphs and Mathematical Tables*, Dover, New York, 1964.

21 H. H. Gan and B. C. Eu, *Phys. Rev. A: At., Mol., Opt. Phys.*, 1992, **45**, 3670.

22 S. Mandal, M. Gross, D. Raabe and F. Varnik, *Phys. Rev. Lett.*, 2012, **108**, 098301.

23 S. Papenkort and T. Voigtmann, *J. Chem. Phys.*, 2014, **140**, 164507.

24 N. Koumakis, M. Laurati, S. U. Egelhaaf, J. F. Brady and G. Petekidis, *Phys. Rev. Lett.*, 2012, **108**, 098303.

25 M. E. Cates, J. P. Wittmer, J.-P. Bouchaud and P. Claudin, *Phys. Rev. Lett.*, 1998, **81**, 1841.

26 J. Mewis and N. J. Wagner, *Colloidal Suspension Rheology*, Cambridge University Press, 2012.